CrossMark

RESEARCH PAPER

Focused surface acoustic wave induced jet formation on superhydrophobic surfaces

Marten Darmawan · Doyoung Byun

Abstract We investigated the unusual droplet jetting formation as a response to the high intensity of a focused acoustic wave on superhydrophobic surface. When focused surface acoustic waves come into contact with a free surface droplet, an elongated pinched liquid column is formed due to the translation of the acoustic radiation force into the inertial body force on the bulk of the droplet. This phenomenon, however, was found to differ as the surface wettability changed. We examined this phenomenon by conducting an experimental observation of the droplet deformation, and a further analysis was carried out using a numerical study, providing a quasi-quantitative analysis of the acoustic radiation pressure distribution.

Keywords Focused surface acoustic wave · Droplet jetting · Surface wettability · Acoustic radiation force

1 Introduction

Since Faraday's first observation in 1831 of liquid interfaces oscillation by vibrating elastic surfaces (Faraday 1831), many attempts have been made to investigate the detail of the underlying physics. The original seminal theoretical work explaining the phenomenon was conducted by Rayleigh, who proposed the theory of elastic surface waves (Rayleigh 1896). Meanwhile, in 1948, Eckart derived

influential hydrodynamic approximations for the acoustic streaming velocity by considering the time-independent gradient of radiation pressure induced by attenuated plane waves in a fluid medium (Eckart 1948).

Surface acoustic wave (SAW) has been known as a potential actuator to manipulate liquid in the microscale regime (Friend and Yeo 2011; Luong et al. 2011; Schmid et al. 2012; Shi et al. 2009; Xuan et al. 2010). Recently, experimental and theoretical works have been conducted to explain and categorize droplet deformation phenomena (which occur due to the interaction of a SAW with a sessile droplet), into several regimes (i.e., oscillation, translation, streaming, jetting, and atomization) (Brunet et al. 2010; Qi et al. 2008; Tan et al. 2009). The characterizations of the regimes depend on the capillary wave characteristic (i.e., viscous-capillary resonance frequency, $f_c = \sqrt{\gamma/\rho R^3}$, where γ is the surface tension of the liquid, ρ is the liquid density, and R is the characteristic length of the droplet) on the interfacial boundary and the streaming velocity on the bulk (which is represented by streaming Reynolds number $\mathrm{Re}_s \equiv \rho U_s R_d/\mu$, where U_s is the streaming velocity, R_d is the radius of droplet, and μ is the liquid viscosity). In addition to that, the explanation of these phenomena also entails the fundamental knowledge of the surface acoustic wave diffraction into a free surface droplet at the Rayleigh angle (Fig. 1a) $\theta_R = \sin^{-1}(c_w/c_s) \approx 22^o$, due to the mismatch of wave propagation speed in water ($c_w = 1,485$ m/s) and substrate ($c_s = 3,965$ m/s). As a result, the acoustic radiation leaks into the droplet and generates a longitudinal pressure wave that induces the recirculation streaming flow (known as the acoustic streaming flow) (Qi et al. 2008). The acoustic streaming force could be explicitly expressed as (Shiokawa et al. 1989)

$$F = -\rho \left(1 + \alpha^2\right)^{3/2} A^2 \omega^2 k_i \exp 2(k_i x + \alpha k_i y)$$

M. Darmawan · D. Byun (✉)
Department of Mechanical Engineering, Sungkyunkwan University, Suwon, Gyeonggi-do 440-746, Republic of Korea
e-mail: dybyun@skku.edu

(a)   **(b)**
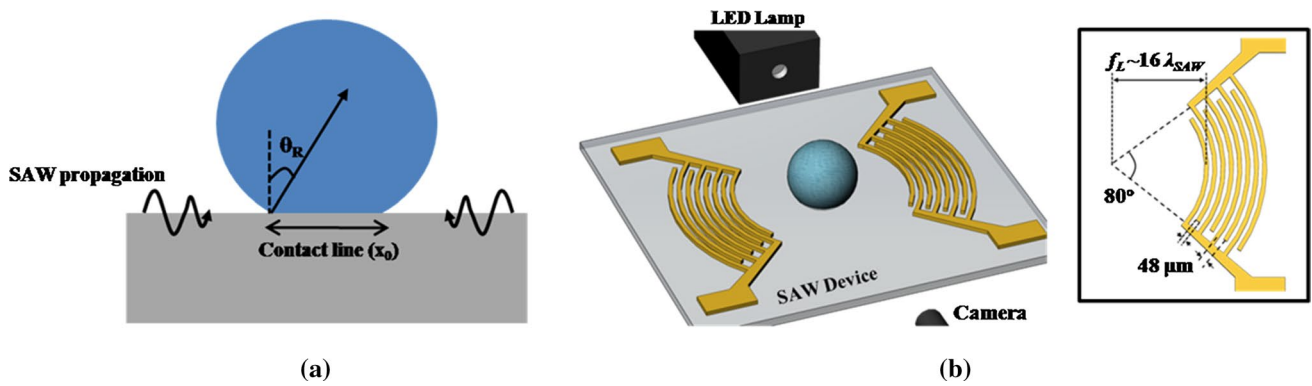
Fig. 1 a Surface acoustic wave diffraction at Rayleigh angle ($\theta_R \approx 22°$) due to the mismatch of wave propagation speed in the substrate and water. **b** Schematic of the experiment, showing the alignment of high-speed camera (3,000 fps), LED source, and SAW device (*inset* focused interdigital transducers specifications for 20 MHz)

where α is the attenuation coefficient, A is the SAW amplitude, ω is the angular frequency, and k_i is the wave number. The effect of frequency on the resulting acoustic streaming force behavior has been extensively explored in a microscale fluid medium (Dentry et al. 2014; Shilton et al. 2014).

Among the abovementioned regimes, a droplet jetting formation was observed and identified as a result once the high intensity of the inertial body force from the focused surface acoustic wave (represented by jetting Weber number, $We_j \equiv \rho U_j^2 R_j / \gamma$, where U_j and R_j are the velocity and radius of the jet, respectively) overcomes the surface tension of the droplet (Tan et al. 2009). In fact, the jetting phenomena would change into a multiple droplet ejection as the input power increases. Until now, the effect of surface wettability has not been studied yet, typically on the superhydrophobic surface.

In this study, we investigated the jetting droplet deformation behavior focusing the effect of surface wettability using high intensity focused surface acoustic waves. Our studies encompassed an experimental observation, a quantitative measurement of the droplet water deformation with varied surface wettability (i.e., hydrophobic and superhydrophobic), and a quasi-quantitative numerical study analysis to explain the resulting unique jetting behavior and provide the basic insight of the underlying droplet deformation mechanism.

2 Experimental method

2.1 Surface acoustic wave device

In our experiment, a concentric circular focused surface acoustic wave (F-SAW) device was designed with the configuration of an 80° arc, 25 pairs of concentric interdigital transducer (IDT) electrodes, and a 20 MHz ($\lambda_{SAW} \approx 198$ μm) resonance frequency. The focal length (f_L) was set at ~16 λ_{SAW} from the outermost finger electrode (Fig. 1b). The F-SAW's design configuration is based on the consideration of using intermediate arc angle and proper focal distance to produce constant amplitude field and obtain stable focusing properties (Wu et al. 2005). The IDTs were fabricated by patterning the Au–Cr electrodes (~200 nm) on a 500-μm-thick 128° Y-cut lithium niobate (LiNbO$_3$) (Yamaju Ceramics Inc., Japan) piezoelectric substrate using a standard UV photolithography process (Darmawan et al. 2014). Furthermore, two different methods were used to modify the surface energy of the substrate into hydrophobic and superhydrophobic. The hydrophobic film (water contact angle ~105 ± 2°) was made by spin coating the Teflon (Teflon AF, Dupont) layer on the substrate at 4,000 rpm and then curing the substrate at 60 °C for 6 h. Meanwhile, a straightforward plasma treatment with a proper gas composition (He, CH$_4$, and C$_4$F$_8$) was used to transform the hydrophilic substrate into a superhydrophobic substrate with a water contact angle of up to ~155 ± 3°.

2.2 Experiment apparatus

The standing focused surface acoustic waves were generated by applying the amplified RF square AC signals (~19.97 MHz) to maximize the V_{rms} values from a function generator (Agilent 33220A) to the interdigital transducers (IDTs). In addition, a fixed −1 dB RF attenuator was used as an impedance to protect the SAW device from the sudden high voltage input and to filter the noise from the RF amplifier (Amplifier Research 150A 100B). The output line was split to the RF power meter (NISSEI TM-4000X) to measure the actual applied forward power on the F-SAW device. Furthermore, a high-speed camera (Photron Inc.,
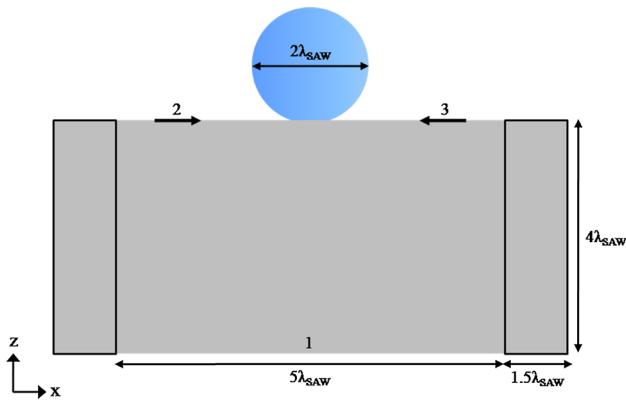
Fig. 2 Numerical configuration of liquid and solid domains. The dimension that is used in this study is based on the surface acoustic wavelength (i.e., $\lambda_{SAW} \approx 198$ µm)

APX-RS, Japan) with mounted zooming lens at 3,000 fps was used in this experiment. Note that a water droplet with a volume 3 ± 0.5 µl was used in all experiment cases. The water droplet was manually placed on the center of the F-SAW device using a micropipette (Acura manual 825 Socorex, Switzerland). Figure 1b depicts the schematic of the experimental observation in this study.

3 Numerical method

In order to explain the droplet jetting formation on both substrates (i.e., hydrophobic and superhydrophobic), we conducted a 2D finite element numerical study using COMSOL Multiphysics 4.4 software with an elastic wave module and frequency domain solver. The unit length of the geometries in our model was based on the fixed surface acoustic wavelength (i.e., $\lambda_{SAW} = c/f_{SAW} \approx 198$ µm) for 20 MHz resonance frequency. The linear elastic and isotropic model was applied to the solid domain, while the thermo-viscous model was used for the pressure acoustic model on the liquid domain.

Figure 2 shows the domain of configuration used in our numerical study. For the solid elastic domain, we defined a finite two-dimensional slab of which the thickness and width were 4 λ_{SAW} and 5 λ_{SAW}, respectively. Furthermore, a hemispherical liquid domain with 2 λ_{SAW} diameter is defined as a liquid drop. In addition, perfectly matched layers (PMLs) with 1.5 λ_{SAW} width and the same thickness as the substrate at the end of both substrates were also used to suppress the reflection wave from the boundary edges. The dimensions were adjusted to produce the optimum approximation to the real phenomena considering favorable computation cost.

The Rayleigh wave was generated by applying a symmetric displacement mode on the elastic solid material

along the excitation nodes (Quintero and Simonetti 2013; Schröder and Scott 2001) at boundary 2 and 3. The explicit expressions of the time harmonic-dependent displacement and stress components are as follows:

$$H_x = \left(j\xi A e^{j\psi z} - j\beta B e^{j\beta z} \right) e^{j\xi x},$$

$$H_z = \left(j\psi A e^{j\psi z} + j\xi B e^{j\beta z} \right) e^{j\xi x},$$

$$\tau_{xx} = \eta \left(\left(2\psi^2 - \beta^2 - \xi^2 \right) A e^{j\psi z} + 2\beta\xi B e^{j\beta z} \right) e^{j\xi x},$$

$$\tau_{zz} = \eta \left(\left(\xi^2 - \beta^2 \right) A e^{j\psi z} - 2\beta\xi B e^{j\beta z} \right) e^{j\xi x},$$

$$\tau_{xz} = \eta \left(-2\psi\xi A e^{j\psi z} + \left(\beta^2 - \xi^2 \right) B e^{j\beta z} \right) e^{j\xi x},$$

and the wave numbers are defined as:

$$\psi^2 = \omega^2/c_p^2 - \xi^2,$$
$$\beta^2 = \omega^2/c_s^2 - \xi^2,$$
$$\xi^2 = \omega^2/c^2,$$

where H_x and H_z are displacement components on x and z direction, c is the Rayleigh wave propagation speed on an solid elastic material, c_p is the pressure wave speed, c_s is the shear wave speed, ω is the frequency (i.e., $2\pi f_{SAW}$), and η is the isotropic elastic Lame constant.

By applying the zero normal stress boundary condition $\tau_{zz}|_{z=0} = \tau_{xz}|_{z=0} = 0$, an A and B coefficient ratio is obtained as follows,

$$\frac{A}{B} = \frac{2\xi\beta}{\xi^2 - \beta^2}$$

Meanwhile, the zero displacement boundary condition was employed at the bottom of the solid domain (i.e., boundary 1). The outer boundaries of the liquid and solid domains were set as pressure- and stress-free conditions. Finally, the continuity of normal stress and displacement was applied on the shared boundary between the liquid and solid domain.

4 Results and discussions

4.1 Droplet deformation on different surface wettability

Figure 3 depicts the time sequence images of the droplet jetting deformation. The image sequence in the top row shows the jetting formation on the hydrophobic surface. Due to the diffraction of SAW directly at the pinning point, the entire liquid droplet was deformed into an elongated jetting formation as the inertial body force started overcoming the surface tension of the droplet. A similar phenomenon was observed and explained by Tan et al. (2009). On the other hand, the image sequence in the bottom row
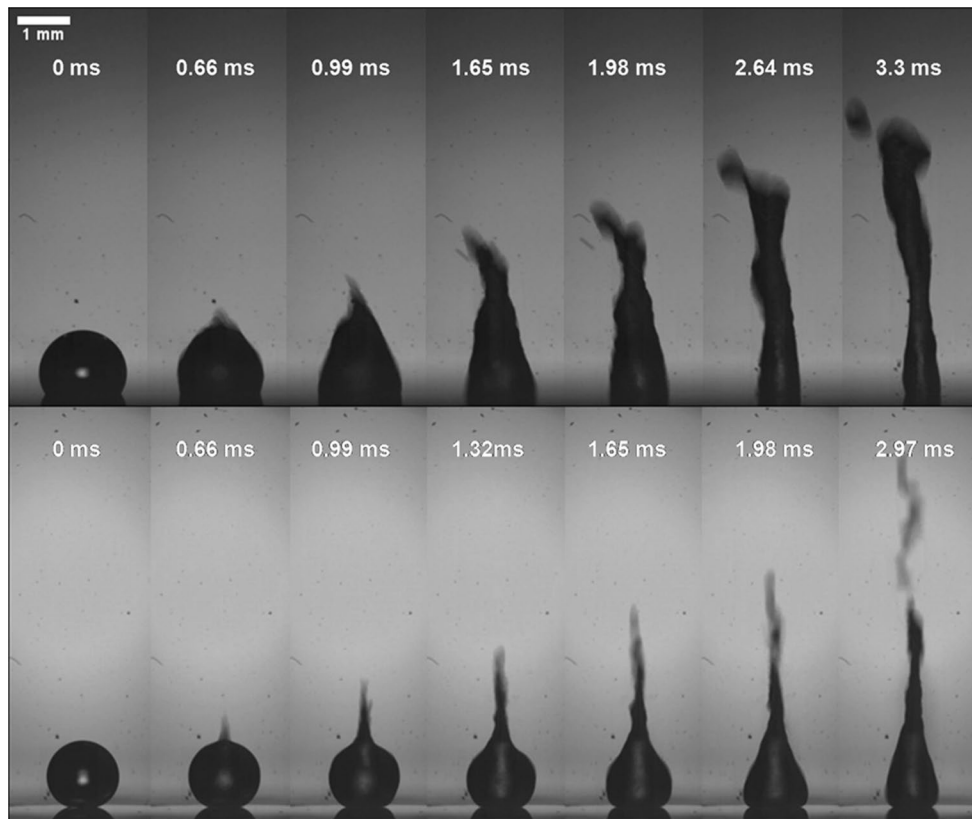
Fig. 3 Image sequences of droplet jetting formation at the same input power (i.e., 12 W). The *top row* image sequence shows the droplet jetting deformation on the hydrophobic substrate (coated with Teflon film ~300 nm thick), while the *bottom row* shows the jetting formation on the superhydrophobic substrate (treated using plasma coating method)

shows an interesting yet unfamiliar droplet jetting formation on the superhydrophobic substrate. A sharp jetting pinching point was instantaneously (i.e., 0.66 ms) formed at the apex of the droplet rather than at the droplet's pinning point. Furthermore, the inertial body force was mostly concentrated on the apex of the droplet and produces an even faster jetting tip speed. The jetting formation therefore progressively changed into multiple jetting due to the high inertial force and small jet radius. The explanation of this peculiar droplet jetting formation was the main focus of the rest of this study. Thus, for a quantitative understanding of the jetting deformation behavior on the superhydrophobic substrate, we conducted a parametrical study by varying the input powers (i.e., 10, 12, and 14 W) that were sufficient to trigger the jetting phenomena but not excessive to damage the F-SAW device, and then compared the results with the hydrophobic case (Fig. 4).

It has been known that the acoustic radiation pressure generates the acoustic streaming flow near the liquid-substrate boundary and destabilizes the contact line equilibrium. This phenomenon, in turn, changes the receding contact angle and induces the depinning phenomenon (Xu and Choi 2012), of which the force per unit length is

$F_d = \gamma(\cos\theta_r - \cos\theta_e)$, where θ_r is the receding contact angle and θ_e is an initial equilibrium contact angle. In this study, to compare the effect on different surface wettability, we quantitatively measured the dynamic change of the droplet contact line from the beginning of the application of the voltage until the droplet sizes shrunk and eventually detached from the substrate in the time frame of 1/3,000 s.

Figure 5 shows the comprehensive results of a dynamic normalized contact line (x_d/x_0) on varied input powers for both hydrophobic and superhydrophobic substrates. In almost all cases, the contact lines were observed to be expanded ~10–60 % during the early deformation stages. The observed droplet expansion might be due to the net contact line force which arises from the hydrodynamics of the local streaming velocity at the viscous boundary layer (Manor et al. 2011). Meanwhile, the result also showed that the input power within the range of 10–14 W does not affect the magnitude of the expansion in hydrophobic case (Fig. 5a). Similarly, the droplet–substrate detach time was approximately the same at any given power within the range. This was probably due to the exceeding input power that overcame the pinning threshold force. However, small and rigid contact line changes were observed at the lowest
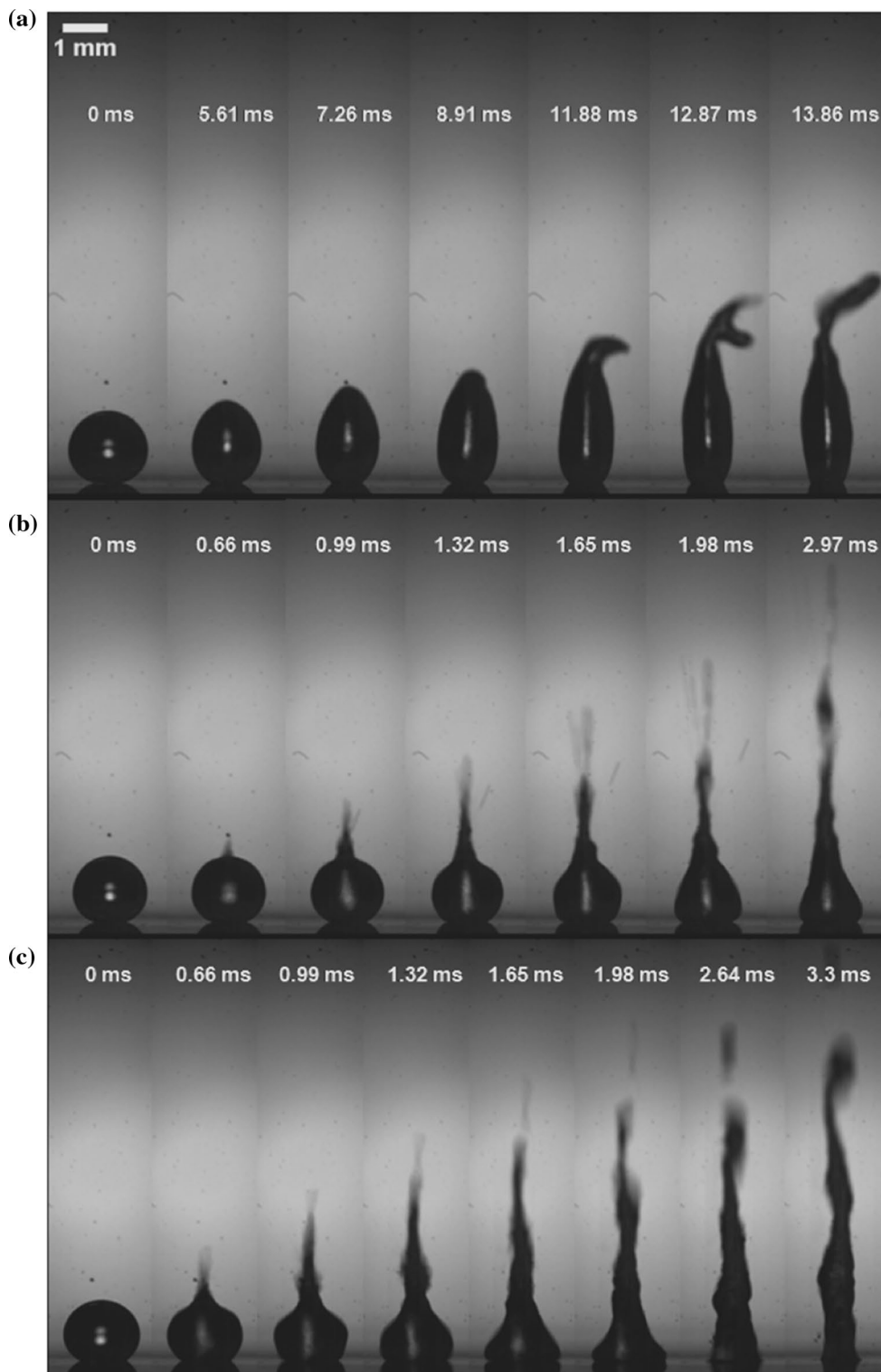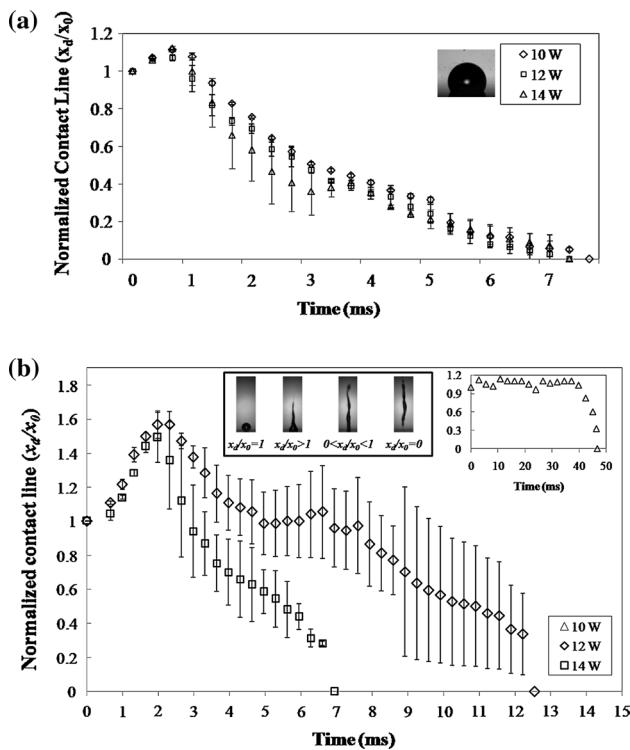
Fig. 4 Droplet deformation on superhydrophobic surface using **a** 10 W, **b** 12 W, and **c** 14 W of input power

input power (i.e., 10 W) on the superhydrophobic substrate as the acoustic radiation force barely overcame the pinning force threshold (Fig. 5b, inset). It should be noted that if the input power was lower than 10 W, it would only induce droplet vibration instead of droplet jetting phenomena, since the bulk body force could not be sufficiently high to cope with the surface tension force. The moderate deviations of contact line dynamics were observed in both

(a)

(b)

Fig. 5 Comparison of the contact line dynamics to show quantitative insight of the droplet depinning phenomenon on **a** hydrophobic and **b** superhydrophobic substrate (*Inset* 10 W). The information on the quantitative contact line changes is represented by normalized contact line (x_d/x_0), where x_d and x_0 are defined as the dynamic contact line and the initial contact line, respectively. The normalized contact line indicates the droplet spreading ($x_d/x_0 > 1$), shrinkage ($0 < x_d/x_0 < 1$), and detachment ($x_d/x_0 = 0$) conditions

of hydrophobic and superhydrophobic cases because the contact line changes were sensitive to the droplet position and its corresponding resonance frequency at a particular

contact area. In fact, the variation becomes more significant on the superhydrophobic surface as the droplet's contact area was significantly small and the position of droplet was also difficult to be precisely maintained at the same spot in every experimental repetition.

Furthermore, the results indicated that the droplet–substrate contact area (regarded as the effective SAW transference area) on different surface wettability would affect the droplet's expansion and detachment time. The contact line dynamics showed that the difference in effective wave propagation contact area slightly affected the acoustic radiation force acting on a droplet. It can be seen from the relatively longer droplet's expansion and detachment time on the superhydrophobic substrate which had smaller effective SAW propagation area compared with the hydrophobic substrate.

4.2 Pressure acoustic wave profile

The acoustic pressure distribution for hydrophobic and superhydrophobic substrates is presented in Fig. 6. The hydrophobic pressure distribution shows a full uniform propagation profile up to the liquid–air interfacial boundary (Fig. 6a). The result contrasts that of the superhydrophobic case, in which the radiation profile is rather concentrated on a narrow trajectory toward the apex of the droplet (Fig. 6b). We argue that one of the essential factors, which induced this distinct disparity, was the contact area at which the leaky surface acoustic wave was propagated and attenuated. The leaky surface acoustic wave was indeed propagated on a longer distance for the hydrophobic case due to the larger wetted liquid–substrate area, thus making its power to decrease smoothly by means of the viscous attenuation mechanism. On the contrary, the smaller contact area on the superhydrophobic substrate lead to a shorter wave
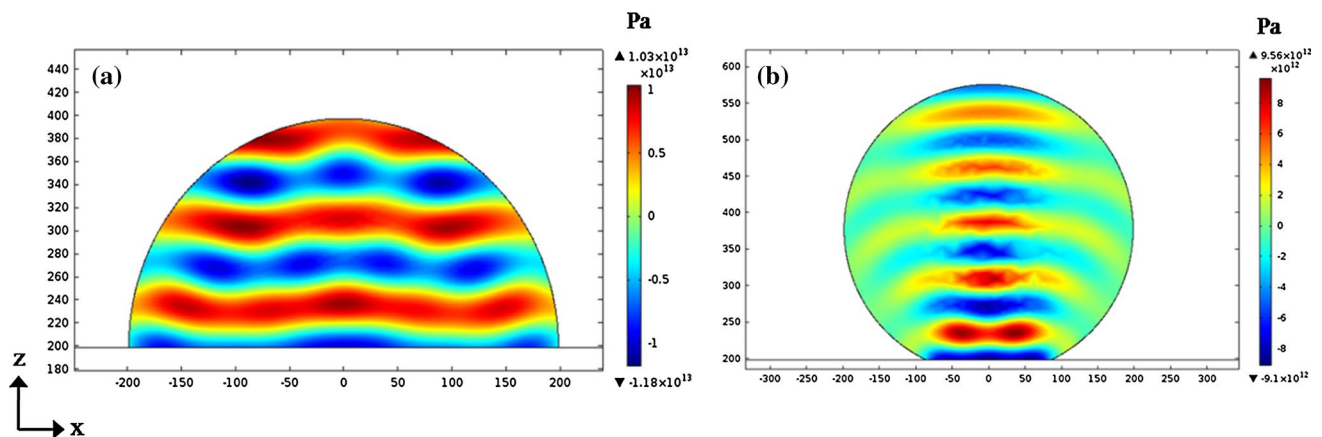
Fig. 6 Numerical study projection of the acoustic radiation pressure distribution profile on **a** hydrophobic (contact angle ~90°) and **b** superhydrophobic substrates (contact angle ~155°). For the geom-

etry, the diameter of the droplet is fixed at $2\lambda_{SAW}$ (λ_{SAW} ~198 μm for 20 MHz resonance frequency) for each case
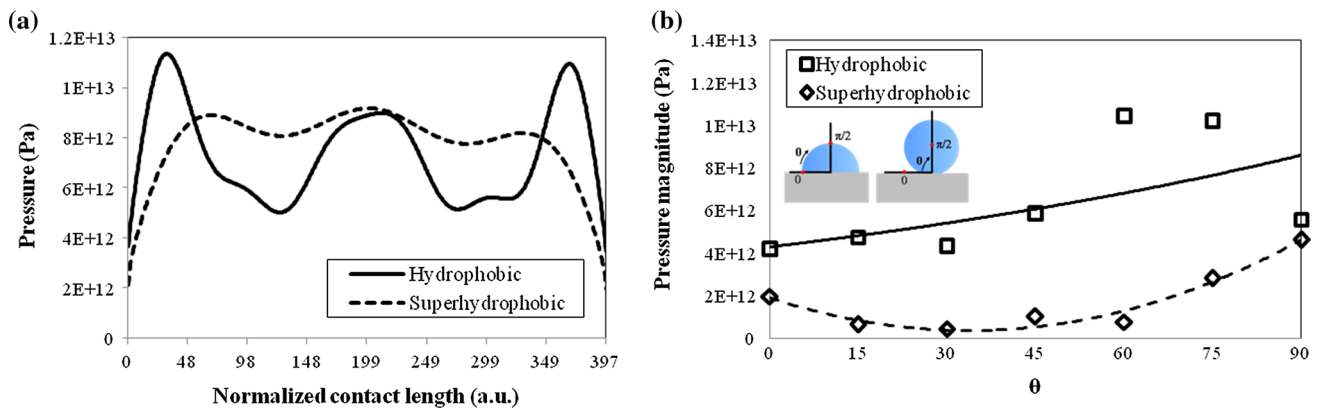
Fig. 7 **a** Comparison of the extracted contact line pressure distribution between hydrophobic and superhydrophobic substrates and **b** the pressure distribution on the water–air interfacial boundary at specified sampling direction angles from the center of droplet from the numerical results. The specified sampling angles were defined differently on hydrophobic and superhydrophobic cases to show balance distribution of sampling points along the half-symmetric axis of the interfacial boundary. Meanwhile, the solid and dashed lines are representing the estimation trends (exponential interpolation function and power law interpolation function, respectively) of the increasing radiation pressure toward the 90° at which the standing wave is formed. The results show the disparity of droplet jetting mechanism on different surface wettabilities (i.e., hydrophobic and superhydrophobic substrates)

propagation path, thus instantly forming a standing wave at the closer center point and hampering the leaky surface wave from being attenuated and expanded uniformly. Therefore, the leaky surface wave was mostly confined to the limited liquid–substrate contact line and propagated on a relatively focused trajectory directly up to the apex of the droplet.

The pressure distribution along the contact line was extracted from the numerical study to clarify the aforementioned hypothesis. Figure 7a shows a comparison of the pressure distribution profile on the normalized contact length between the hydrophobic and superhydrophobic substrates. The results show approximately the same trend as that of our prediction in both cases. The contact line pressure distribution on the hydrophobic substrate showed a reasonable pressure profile following the surface acoustic wave diffraction pattern as it leaked into the droplet. The trend showed declining pressure patterns toward the center of the droplet and the creation of a standing wave as the symmetric surface waves meet at the center of the droplet. Meanwhile, a relatively flat pressure distribution profile was observed on the superhydrophobic substrate as a result of a shorter surface wave propagation distance and the near meeting point of the symmetric surface wave. This result emphasized that the lack of propagation distance would lead to the creation of focused and localized pressure distribution. In addition, it should be noted that the volume-average radiation pressure on the superhydrophobic substrate, from the view of numerical study, was ~25 % lower than that on the hydrophobic substrate due to the slightly bigger defined droplet volume. However, the difference was not affecting the resulted acoustic radiation pressure profile.

4.3 Interfacial pressure distribution

The deformation of the shape of the droplet to a jetting formation is also related to the pressure distribution on the liquid–vapor interfacial boundary that is responsible for triggering the capillary waves. This interfacial pressure energetically destabilizes the equilibrium of the droplet's hydrostatic pressure, which is defined as $\Delta p = 2\gamma/R$, where R is the radius of a spherical droplet. Note that the surface tension, which is determined by the surface energy balance (De Gennes 1985) $\gamma_{SV} = \gamma_{SL} + \gamma_{LV}\cos\theta$, would also retain the natural droplet shape during the creation of the capillary wave on the interfacial boundary. We therefore traced the half-symmetric pressure distribution along the droplet's interfacial boundary at specified angles (Fig. 7b). The results concur with the preceding arguments which reveal the disparities of the pressure distribution profiles throughout a droplet on both substrate conditions (i.e., hydrophobic and superhydrophobic). The trend of the interfacial pressure distribution on the hydrophobic substrate reasonably followed the prior pressure distribution profile of the bulk. At the small angle, the interfacial pressure was fairly low as the instantaneous radiation pressure diffraction was directed and perpetually advanced at the specified Rayleigh angle. On the other hand, the interfacial pressure level in the superhydrophobic case was consistently small at low angles, meaning that the radiation pressure is localized at the contact line. However, at the apex of the droplet (i.e., 90°), the interfacial pressure is at a maximum due to the emergence of a standing wave at the center of the droplet.

5 Conclusion

In conclusion, we conducted an experimental observation and a numerical study of the peculiar droplet jetting deformation on varied substrate wettability (i.e., hydrophobic and superhydrophobic). The distinct pressure distribution comparison revealed the disparity of the jetting characteristic. Through a preliminary quasi-analytical numerical study, it is demonstrated that the peculiar jetting mechanism on the superhydrophobic substrate is induced by a focused and localized pressure radiation profile, which distinguishes it from the hydrophobic substrate. It should also be noted that the jetting deformation is also affected by the depinning mechanism from which the leaky surface acoustic wave could be transferred at the dynamic changes of the contact line.

References

Brunet P, Baudoin M, Matar OB, Zoueshtiagh F (2010) Droplet displacements and oscillations induced by ultrasonic surface acoustic waves: a quantitative study. Phys Rev E 81:036315

Darmawan M, Jeon K, Ju JM, Yamagata Y, Byun D (2014) Deposition of poly (3, 4-ethylenedioxythiophene)–poly (styrenesulfonate) (PEDOT-PSS) particles using standing surface acoustic waves and electrostatic deposition method for the rapid fabrication of transparent conductive film. Sens Actuators A 205:177–185

De Gennes P-G (1985) Wetting: statics and dynamics. Rev Mod Phys 57:827

Dentry MB, Yeo LY, Friend JR (2014) Frequency effects on the scale and behavior of acoustic streaming. Phys Rev E 89:013203

Eckart C (1948) Vortices and streams caused by sound waves. Phys Rev 73:68

Faraday M (1831) On a peculiar class of acoustical figures; and on certain forms assumed by groups of particles upon vibrating elastic surfaces. Philos Trans R Soc Lond 121:299–340

Friend J, Yeo LY (2011) Microscale acoustofluidics: Microfluidics driven via acoustics and ultrasonics. Rev Mod Phys 83:647

Luong T-D, Phan V-N, Nguyen N-T (2011) High-throughput micromixers based on acoustic streaming induced by surface acoustic wave. Microfluid Nanofluidics 10:619–625

Manor O, Dentry M, Friend JR, Yeo LY (2011) Substrate dependent drop deformation and wetting under high frequency vibration. Soft Matter 7:7976–7979

Qi A, Yeo LY, Friend JR (2008) Interfacial destabilization and atomization driven by surface acoustic waves. Phys Fluids (1994-present) 20:074103

Quintero R, Simonetti F (2013) Rayleigh wave scattering from sessile droplets. Phys Rev E 88:043011

Rayleigh JWSB (1896) The theory of sound, vol 2. Macmillan, Newyork

Schmid L, Wixforth A, Weitz DA, Franke T (2012) Novel surface acoustic wave (SAW)-driven closed PDMS flow chamber. Microfluid Nanofluid 12:229–235

Schröder CT, Scott WR Jr (2001) On the complex conjugate roots of the Rayleigh equation: the leaky surface wave. J Acoust Soc Am 110:2867–2877

Shi J, Huang H, Stratton Z, Huang Y, Huang TJ (2009) Continuous particle separation in a microfluidic channel via standing surface acoustic waves (SSAW). Lab Chip 9:3354–3359

Shilton RJ, Travagliati M, Beltram F, Cecchini M (2014) Nano-liter-droplet acoustic streaming via ultra high frequency surface acoustic waves. Adv Mater 26(29):4941–4946

Shiokawa S, Matsui Y, Ueda T (1989) Liquid streaming and droplet formation caused by leaky Rayleigh waves. In: Ultrasonics Symposium, 1989. Proceedings., IEEE 1989, pp 643–646

Tan MK, Friend JR, Yeo LY (2009) Interfacial jetting phenomena induced by focused surface vibrations. Phys Rev Lett 103:024501

Wu T-T, Tang H-T, Chen Y-Y, Liu P-L (2005) Analysis and design of focused interdigital transducers. IEEE Trans Ultrason Ferroelectr Freq Control 52:1384–1392

Xu W, Choi C-H (2012) From sticky to slippery droplets: dynamics of contact line depinning on superhydrophobic surfaces. Phys Rev Lett 109:024504

Xuan X, Zhu J, Church C (2010) Particle focusing in microfluidic devices. Microfluid Nanofluidics 9:1–16